IOP PUBLISHING JOURNAL OF PHYSICS D: APPLIED PHYSICS

J. Phys. D: Appl. Phys. **42** (2009) 185206 (7pp) doi:10.1088/0022-3727/42/18/185206

Three-dimensional simulation of a microplasma pump

Chin-Cheng Wang and Subrata Roy

Computational Plasma Dynamics Laboratory and Test Facility, Applied Physics Research Group, Department of Mechanical and Aerospace Engineering, University of Florida, Gainesville, FL 32611, USA

E-mail: roy@ufl.edu

Received 6 May 2009, in final form 27 July 2009
Published 4 September 2009
Online at stacks.iop.org/JPhysD/42/185206

Abstract

We present a three-dimensional simulation of dielectric barrier discharge (DBD) using the finite element based multiscale ionized gas (MIG) flow code. The two-species hydrodynamic plasma model coupled Poisson equation and Navier–Stokes equation are solved using MIG flow code to predict complicated flow structure inside a plasma induced micropump. The advantage of such a micropump is rapid on/off switching without any moving parts. Results show a reasonable distribution for ion and electron densities as well as an electric field. The key factors of microplasma pump design are the location of actuators and input voltage. The flow rate of the microplasma pump is on the order of ml min^{-1}. Such a flow rate may be beneficial for micropropulsion in space.

(Some figures in this article are in colour only in the electronic version)

1. Introduction

Mircopump is made by fabrication on the order of micrometres to draw or drain the working fluid in the microfluidic system, such as lab-on-a-chip (LOC) or a micro total analysis system (μTAS). Since its introduction in the mid-1970s [1], micropumps are becoming widely popular in a variety of applications ranging from biological analysis and chemical detection to space exploration and microelectronics cooling. A variety of micropumps have been developed based on the operational mechanism. These may be categorized as mechanical and non-mechanical devices. The mechanical micropumps drive the working fluid through a membrane or diaphragm, while the non-mechanical micropumps inject momentum or energy into a local region to produce pumping operation. Based on the motion of mechanical micropumps, it can be divided into reciprocating, rotary and aperiodic pumps. Mechanical micropumps include electrostatic, pneumatic, thermopneumatic, piezoelectric and electromagnetic diaphragm pumps. Diaphragm pumps can be used for any gas or liquid and generate flow rates in the range of ml min^{-1}. However, the drawbacks are the relatively high cost and the short lifetime of the moving diaphragm due to their frequently on/off switching. In contrast, the primary advantage of non-mechanical micropumps is the absence of moving parts. Furthermore, the simple design of such pumps may reduce the cost and increase miniaturization, so that it improves the integration into the microfluidic system. Non-mechanical micropumps include electrohydrodynamic (EHD), electro-osmotic and magnetohydrodynamic pumps. A thorough review of the actuation mechanism and the applications of micropumps have been described by Laser and Santiago [2] and Oh and Ahn [3].

Roy [4] presented a concept of EHD micropump using dielectric barrier discharge (DBD) actuators shown in figure 1. Such design leverages several advantages of non-mechanical micropumps. Over the last decade, many experiments and numerical simulation show that DBD actuators produce effects on drag reduction inside the boundary layer [5–9]. However, these traditional macroscale DBD actuators suffer from relatively small actuation at high speed flow (>30 m s^{-1}). As a remedy, microscale plasma actuators may induce orders of magnitude higher force density [10].

Microscale plasma discharge has been studied both experimentally and numerically for more than a decade [10–20]. However, there is still room for understanding of the fundamental physics in reduced length scale, the unsteady phenomena and the interaction between plasma and gas in a microgap. In experiment, Wilson *et al* [13] showed that nitrogen microdischarge can be generated within

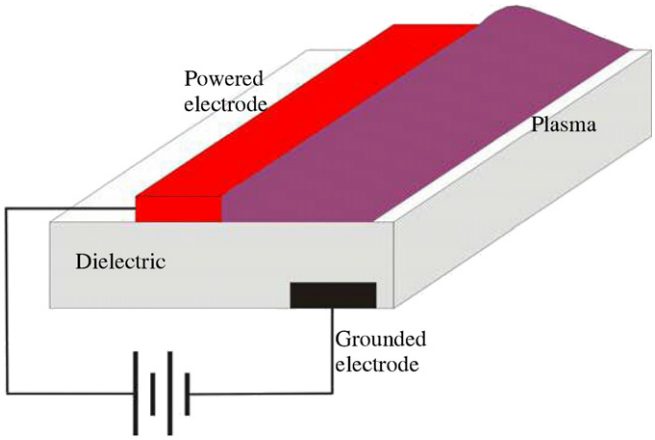

Figure 1. Schematic of the asymmetric single dielectric barrier plasma actuator.

4 mm at 1.5 Torr and 0.4 mm at 10 Torr. The electric fields in this glow region are 100 kv m^{-1} at 1.2 Torr and 500 kv m^{-1} at 6 Torr. Such low pressure microplasma has evolved into plasma-enhanced chemical vapour deposition for microelectromechanical system and integrated circuit processing. Several numerical investigations of microscale discharge generally fall into three major categories. (1) The *hydrodynamic model*, which is based on conservation of mass and momentum [14–17]. It is the most popular model due to its effective capturing of the overall physics at a low computational cost. (2) The *kinetic model*, which is the particle-in-cell/Monte Carlo collision (PIC/MCC) model [18, 19]. (3) The *hybrid kinetic–fluid simulation model*, which solves the reaction rates from the Monte Carlo collision model and then brings the solutions into the hydrodynamic model to get the plasma physics [20]. In the hydrodynamic model, Kushner [14] found a microscale discharge obeying Paschen's curve for breakdown. Sakiyama and Graves [15] presented a two-dimensional (2D) finite element based neutral gas and RF plasma model for solving needle discharge under atmospheric pressure. They found that the ion wind and gas heating have minor effects on the discharge.

Our recent 2D hydrodynamic model of microscale direct current (dc) volume discharge [10] shows very good agreement with published experimental data. The results mimic the trend at both macro and microscale discharges, but the sheath structure dominated the plasma region at certain values of the microgap. The force density is also found to be three orders of magnitude higher than the macroplasma actuator. However, the net flow inducement remains similar to that of a standard actuator due to orders of magnitude smaller plasma region than the traditional counterparts. A 2D microplasma pump model was simulated for the plasma–gas interactions predicting a reasonable 28.5 ml min^{-1} average flow rate of nitrogen gas. However, such 2D models are limited especially for a three-dimensional (3D) geometry. Thus, for a better design of the microplasma pump, it is important to identify 3D effects on plasma and gas flow fields. To our knowledge, the reported numerical results of plasma simulation are either one or two dimensional. So far, very little work has been done on 3D simulation of microscale plasma based devices.

In this paper, we extend our 2D hydrodynamic model [8, 10, 21] into the 3D dc plasma simulation. The charge density q ($= n_\mathrm{i} - n_\mathrm{e}$) and electric field $\boldsymbol{E}$ will be solved based on the first principles. The obtained electric force density ($\boldsymbol{F} = eq\boldsymbol{E}$) from plasma simulation will be employed as a local body force term in the Navier–Stokes equation. Section 2 provides the governing equations for plasma and fluid flow. Section 3 gives two different designs of microplasma pumps. Section 4 shows the results of microplasma pumps for two cases. Conclusions are summarized in section 5.

2. Numerical model

We extend the 2D two-species hydrodynamic plasma formulation of Kumar and Roy [21] into a 3D model for microplasma pump simulation. The unsteady transport for ions and electrons is derived from first principles in the form of conservation of species continuity and the species momentum flux embedded in them using the drift-diffusion approximation under isothermal condition. Such an approximation can predict the general characteristics of plasma discharges in the pressure range from 1 to 50 Torr [22]. The continuity equations for concentration of positive ion n_i and electron n_e together with the Poisson equation for electric field vector $\boldsymbol{E}$ (E_x, E_y, E_z) are

$$\begin{aligned}
&\frac{\partial n_\mathrm{i}}{\partial t} + \nabla\cdot(n_\mathrm{i}\boldsymbol{V}_\mathrm{i}) = \alpha\,|\Gamma_\mathrm{e}| - r n_\mathrm{i} n_\mathrm{e},\\
&\frac{\partial n_\mathrm{e}}{\partial t} + \nabla\cdot(n_\mathrm{e}\boldsymbol{V}_\mathrm{e}) = \alpha\,|\Gamma_\mathrm{e}| - r n_\mathrm{i} n_\mathrm{e},\\
&|\Gamma_\mathrm{e}| = \sqrt{(n_\mathrm{e}V_\mathrm{e})_x^2 + (n_\mathrm{e}V_\mathrm{e})_y^2 + (n_\mathrm{e}V_\mathrm{e})_z^2},\\
&\nabla\cdot(\varepsilon\boldsymbol{E}) = -e\,(n_\mathrm{e} - n_\mathrm{i})\,,
\end{aligned} \tag{1}$$

where n_e and n_i are number densities of electron and ion, respectively, $\boldsymbol{V}$ (V_x, V_y, V_z) is the species hydrodynamic velocity, $r \sim 2\times10^{-7}$ cm^3 s^{-1} is the electron–ion recombination rate, ε is the dielectric constant, the elementary charge e is 1.6022×10^{-19} C and subscripts i and e are positive ion and electron, respectively. The working gas is nitrogen at 5 Torr. The discharge is maintained using a Townsend ionization scheme. The production from ionization is expressed as a function of electron flux $|\Gamma_\mathrm{e}|$ and the Townsend coefficient α:

$$\alpha = A\,p\,\exp\left(-B/\left(|\boldsymbol{E}|/p\right)\right), \tag{2}$$

where $A = 12$ cm^{-1} Torr^{-1} and $B = 342$ V cm^{-1} Torr^{-1} are pre-exponential and exponential constants, respectively, p is the gas pressure and $\boldsymbol{E}$ is the electric field. The ionic and electronic fluxes without magnetic field effect in equation (1) are written as

$$\begin{aligned}
&n_\mathrm{i}\boldsymbol{V}_\mathrm{i} = n_\mathrm{i}\mu_\mathrm{i}\boldsymbol{E} - D_\mathrm{i}\nabla n_\mathrm{i},\\
&n_\mathrm{e}\boldsymbol{V}_\mathrm{e} = -n_\mathrm{e}\mu_\mathrm{e}\boldsymbol{E} - D_\mathrm{e}\nabla n_\mathrm{e}.
\end{aligned} \tag{3}$$

Finally, we end up with the following equations:

$$\frac{\partial n_\mathrm{i}}{\partial t} + \frac{\partial}{\partial x}\left\{n_\mathrm{i}\mu_\mathrm{i}E_x - D_\mathrm{i}\frac{\partial n_\mathrm{i}}{\partial x}\right\} + \frac{\partial}{\partial y}\left\{n_\mathrm{i}\mu_\mathrm{i}E_y - D_\mathrm{i}\frac{\partial n_\mathrm{i}}{\partial y}\right\} + \frac{\partial}{\partial z}\left\{n_\mathrm{i}\mu_\mathrm{i}E_z - D_\mathrm{i}\frac{\partial n_\mathrm{i}}{\partial z}\right\} = \alpha\,|\Gamma_\mathrm{e}| - r n_\mathrm{i} n_\mathrm{e},$$

$$\frac{\partial n_\mathrm{e}}{\partial t} + \frac{\partial}{\partial x}\left\{-n_\mathrm{e}\mu_\mathrm{e}E_x - D_\mathrm{e}\frac{\partial n_\mathrm{e}}{\partial x}\right\} + \frac{\partial}{\partial y}\left\{-n_\mathrm{e}\mu_\mathrm{e}E_y - D_\mathrm{e}\frac{\partial n_\mathrm{e}}{\partial y}\right\} + \frac{\partial}{\partial z}\left\{-n_\mathrm{e}\mu_\mathrm{e}E_z - D_\mathrm{e}\frac{\partial n_\mathrm{e}}{\partial z}\right\} = \alpha\,|\Gamma_\mathrm{e}| - r n_\mathrm{i} n_\mathrm{e}, \quad (4)$$

where $\mu_\mathrm{i} = 1.45 \times 10^3/p$ (cm^2 s^{-1} V^{-1}) is the ion mobility, $\mu_\mathrm{e} = 4.4 \times 10^5/p$ (cm^2 s^{-1} V^{-1}) is the electron mobility, D_i and D_e are the ion and electron diffusion coefficients calculated from the Einstein relation which is a function of ion and electron mobility as well as ion and electron temperature, i.e. $D_\mathrm{i} = \mu_\mathrm{i}T_\mathrm{i}$ and $D_\mathrm{e} = \mu_\mathrm{e}T_\mathrm{e}$. The electric field is given by $\boldsymbol{E} = -\nabla\varphi$, i.e. the gradient of electric potential φ. The system of equation (1) is normalized using the following normalization scheme: $\tau = t/t_0$, $z_\mathrm{i} = x_\mathrm{i}/d$, $N_\mathrm{e} = n_\mathrm{e}/n_0$, $N_\mathrm{i} = n_\mathrm{i}/n_0$, $u_\mathrm{e} = V_\mathrm{e}/V_\mathrm{B}$, $u_\mathrm{i} = V_\mathrm{i}/V_\mathrm{B}$ and $\phi = e\varphi/k_\mathrm{B}T_\mathrm{e}$, where k_B is Boltzmann's constant, $V_\mathrm{B} = \sqrt{k_\mathrm{B}T_\mathrm{e}/m_\mathrm{i}}$ is the Bohm velocity, reference length d which is usually a domain characteristic length in the geometry, the reference time $t_0 = 10^{-8}$ s and reference density $n_0 = 10^{15}$ m^{-3}.

Nitrogen gas is governed by the conservation of mass as

$$\frac{\partial \rho}{\partial t} + \nabla\cdot(\rho V_\mathrm{n}) = 0, \quad (5)$$

where ρ is the fluid density and subscript n denotes the working nitrogen gas. The second term can be further decomposed via the chain rule:

$$\frac{\partial \rho}{\partial t} + V_\mathrm{n}\cdot\nabla\rho + \rho\nabla\cdot V_\mathrm{n} = \frac{\mathrm{D}\rho}{\mathrm{D}t} + \rho\nabla\cdot V_\mathrm{n} = 0. \quad (6)$$

For incompressible flow, the characteristic velocity V_n must be much smaller than the speed of sound c, i.e. Mach numbers $Ma = V_\mathrm{n}/c$ below approximately 0.3, and the compressible effect can be neglected. For the incompressible fluid (ρ =constant, $D\rho/Dt = 0$) is $\nabla\cdot V_\mathrm{n} = 0$.

The conservation of momentum may be derived from Newton's second law as follows:

$$\rho\frac{\mathrm{D}V_\mathrm{n}}{\mathrm{D}t} = \boldsymbol{F} + \nabla\cdot\sigma, \quad (7)$$

where $\boldsymbol{F} = eq\boldsymbol{E}$ is the body force and $\sigma = -\nabla p + \nabla\cdot[-\frac{2}{3}\mu(\nabla\cdot V_\mathrm{n})] + \nabla\cdot(2\mu\varsigma)$ is the stress tensor, where p is the pressure, μ is the viscosity of fluid and ς is the strain rate tensor. For an incompressible Newtonian fluid, the Navier–Stokes equation is

$$\rho\frac{\mathrm{D}V_\mathrm{n}}{\mathrm{D}t} = eq\boldsymbol{E} - \nabla p + \mu\nabla^2 V_\mathrm{n}. \quad (8)$$

In the microscale regime, the continuum approach with the no-slip boundary condition may not hold when the Knudsen number is greater than 0.1 as shown in table 1 [23]. The non-dimensional Knudsen number is defined as the ratio of the fluid mean free path λ and the macroscopic characteristic length Λ, i.e. $Kn = \lambda/\Lambda$. As Kn increases, the rarefaction effects become more dominant between the bulk of the fluid and the wall surface. For conditions stated in this paper, the Kn is less than 0.024 validating the use of the no-slip condition.

Table 1. Different regimes of fluid flow depending on the Knudsen number [23].

Range, Kn	Flows	Equations
0–10^{-2}	Continuum flow	No-slip Navier–Stokes
10^{-2}–10^{-1}	Slip flow	Slip Navier–Stokes
10^{-1}–10^{1}	Transition flow	Burnett equations
10^{1}–∞	Free-molecule flow	Boltzmann equations

The numerical model for solving the DBD plasma and the Navier–Stokes equations uses an efficient finite element algorithm for solving partial differential equations (PDE) approximately. The solution methodology anchored in the modular multiscale ionized gas (MIG) flow code is based on the Galerkin weak statement (GWS) of the PDE [24] which is derived from variational principles. An iterative sparse matrix solver called generalized minimal residual (GMRES) is utilized to solve the resultant stiff matrix. The fully implicit time stepping procedure along with the Newton–Raphson scheme is used for dealing with this non-linear problem. The solution is assumed to have converged when the L_2 norms of all the normalized solution variables and residuals are below a chosen convergence criterion of 10^{-3}.

3. Problem description

Figure 2 shows a schematic of the microplasma pump: (*a*) cross-section and (*b*) the isometric view. We can see that this tri-directional plasma pump draws the fluid into the microchannel at both the inlets due to the attraction of parallel plasma actuators and drains the fluid upwards to the outlet by means of horseshoe plasma actuators. Two cases described in table 2 were simulated. The inlet openings of the pump for both cases are 0.1296 mm^2, while the outlet openings are 0.24 mm^2 for case 1 and 0.39 mm^2 for case 2. The volume of the microplasma pump is 2 mm^3. The length and the width of the electrodes are 200 μm and 12.5 μm for the parallel actuator. The horseshoe actuator consists of two semi-circle electrodes with an inner arc radius of 0.25 μm. We neglect the thickness of the electrodes in the vertical z-direction. The gap between the electrodes is 50 μm in the streamwise x-direction and 24 μm in the vertical z-direction which is also the dielectric thickness. We simulate the symmetric half of these microplasma pumps to reduce computational cost.

Figure 3 shows the computational mesh in 2D cross-section and 3D domain for case 1 (figure 3(*a*)) and case 2 (figure 3(*b*)). The domain size consists of 96 × 48 × 60 tri-linear elements with 289 933 nodes. The mesh density is of the order of Debye length which is sufficient to capture the physics of plasma dynamics. Figure 3(*a*) shows the locations of all the actuators in a 2D cross-section for case 1. The powered

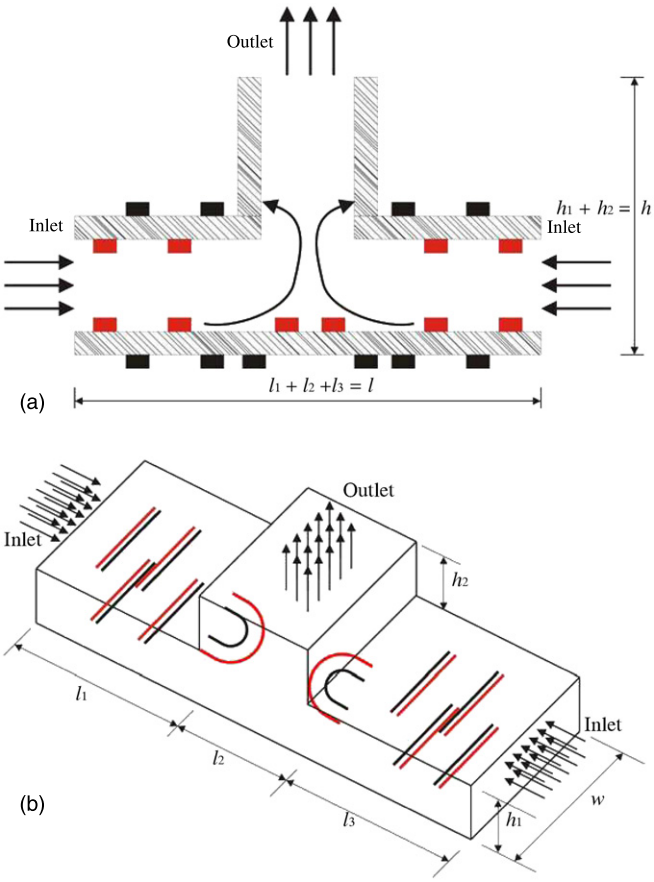

Figure 2. Schematic of microplasma pump: (*a*) cross-section and (*b*) isometric view. (Colour online.)

Table 2. Geometric parameter for two simulated cases.

Unit: mm	l_1	l_2	l_3	h_1	h_2	W
Case 1	1	0.4	1	0.216	0.144	0.6
Case 2	0.875	0.65	0.875	0.216	0.144	0.6

electrodes (red colour) are from $x = 0.25$ to 0.2625 mm, from $x = 0.6$ to 0.6125 mm and from $x = 1.375$ to 1.5 mm. The dielectric surface is Teflon film between electrodes from $z = 0$ to 0.024 mm and from $z = 0.216$ to 0.24 mm. The grounded electrodes (black colour) are from $x = 0.3125$ to 0.325 mm, from $x = 0.6625$ to 0.675 mm and from $x = 0.975$ to 0.9875 mm. The mesh densities of case 2 and case 1 are the same as shown in figure 3(*b*), but the location of the actuators and the size of the outlet opening are different. For the plasma boundary conditions, dc potential is applied to the powered electrode of $\phi = 50$ V for case 1 and $\phi = 80$ V for case 2. For the fluid flow boundary conditions, we assume zero pressure ($p = 0$) at the inlet and the outlet and no-slip condition on the dielectric surface for all three velocity components V_x, V_y and V_z for both cases. We assume symmetric boundary condition at $x = 1.2$ mm which is the centre of the microplasma pump.

4. Results and discussion

Two different outlet openings and applied potential of microplasma pumps are simulated. The results of case 1

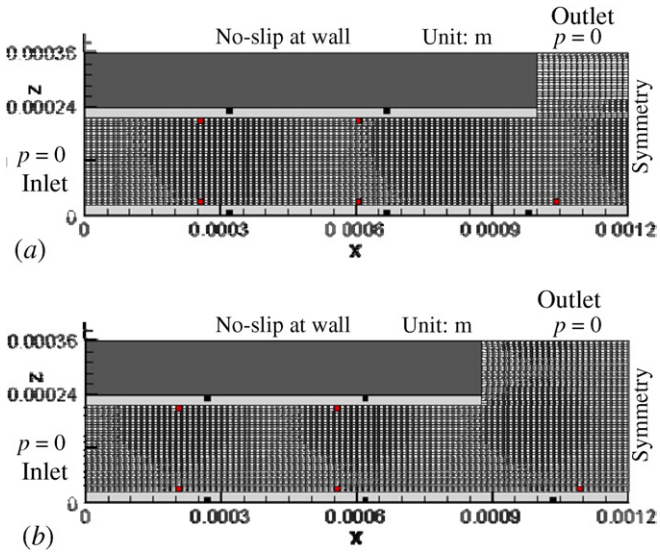

Figure 3. Computational mesh density for (*a*) cross-section of case 1, (*b*) cross-section of case 2. (Colour online.)

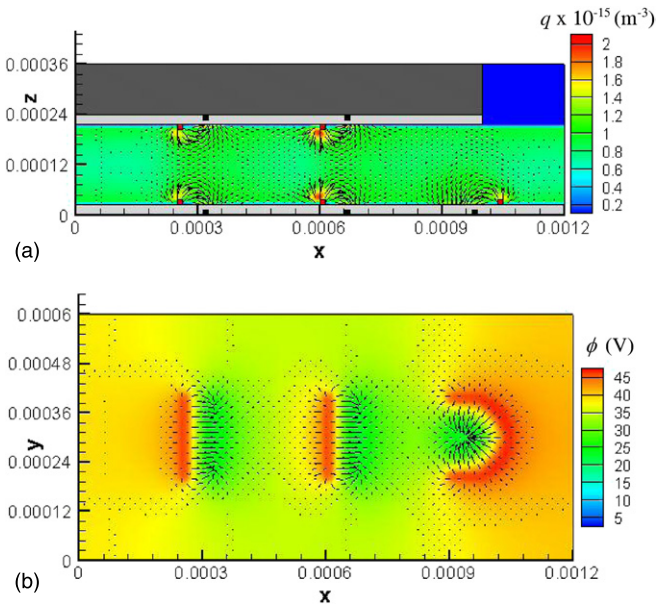

Figure 4. Case 1: (*a*) charge separation $q = n_i - n_e$ at x–z plane ($y = 0.3$ mm) and (*b*) potential distribution at x–y plane ($z = 0.03$ mm) with force vectors. (Colour online.)

are shown in figures 4 and 5, while the results of case 2 are shown in figures 6 and 7. For plasma simulation, ion and electron densities are solved using the two-species hydrodynamic model coupled with the Poisson equation described in equation (1). The ions and electrons are formed through the impact ionization process. The recombination is also considered for the time averaged ion and electron densities. Due to the large time scale difference between plasma and fluid flow, we assume flow dynamics does not affect plasma dynamics and only consider plasma actuation of the fluid.

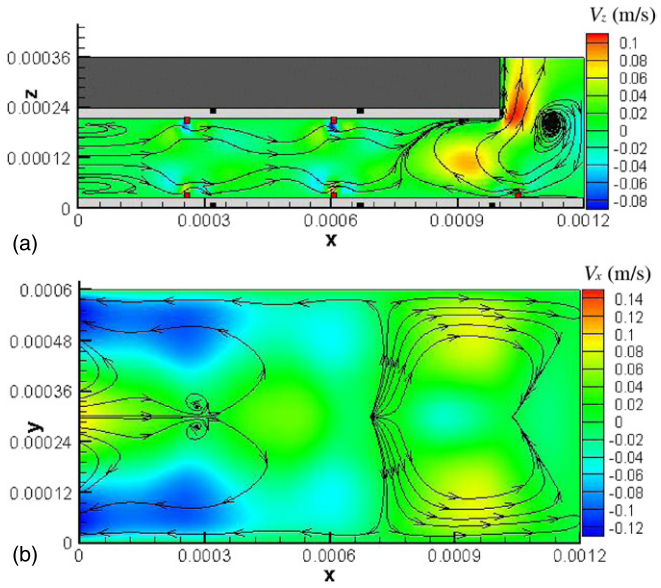

Figure 5. Case 1: (*a*) V_z-velocity contour at x–z plane ($y = 0.3$ mm) and (*b*) V_x-velocity contour at x–y plane ($z = 0.12$ mm) with stream traces. (Colour online.)

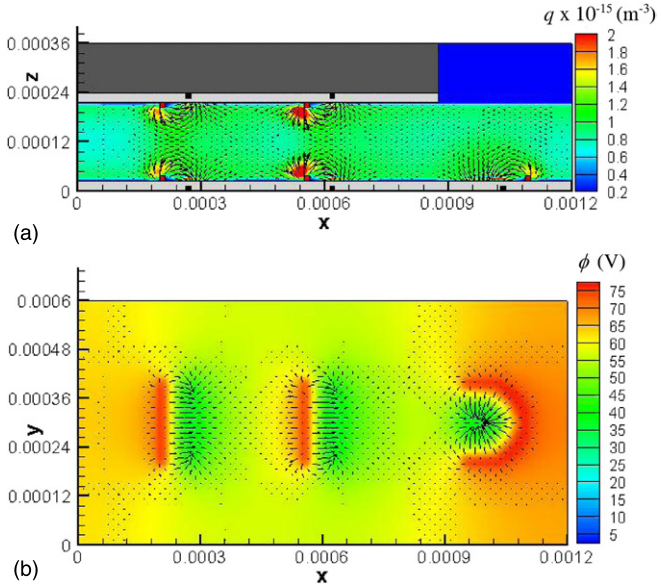

Figure 6. Case 2: (*a*) charge separation $q = n_i - n_e$ at x–z plane ($y = 0.3$ mm) and (*b*) potential distribution at x–y plane ($z = 0.03$ mm) with force vectors. (Colour online.)

4.1. Case 1: small opening with 50 V

Figure 4 shows the charge separation at $y = 0.3$ mm and potential contour plot at $z = 0.03$ mm with force vectors. The charge separation is given by $q = n_i - n_e$ as shown in figure 4(*a*). The peak of charge separation is close to the powered electrode. The strongest force vectors are also close to the powered electrode because the time average of electrostatic force per volume ($\boldsymbol{F} = eq\boldsymbol{E}$) is a function of charge separation and electric field. We can also see that the force vectors are acting from the powered electrode to the grounded electrode which matches the electric field lines shown. The potential distribution is solved by the Poisson equation and matches the boundary condition from 50 to 0 V as shown in figure 4(*b*).

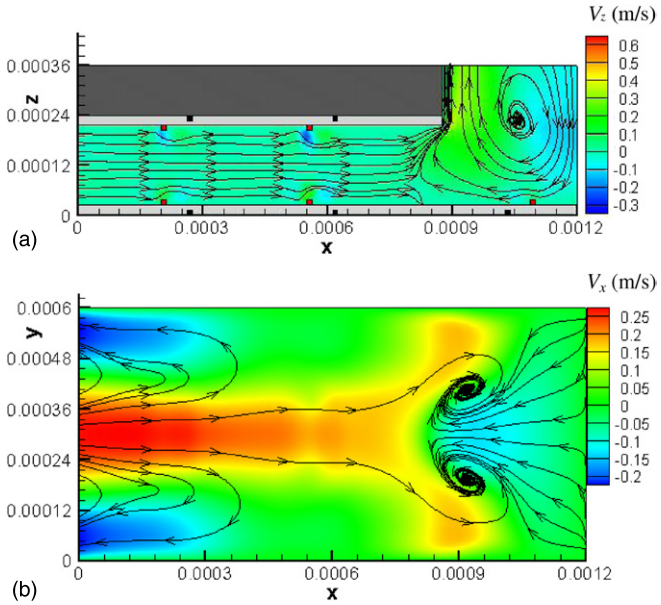

Figure 7. Case 2: (*a*) V_z-velocity contour at x–z plane ($y = 0.3$ mm) and (*b*) V_x-velocity contour at x–y plane ($z = 0.12$ mm) with stream traces. (Colour online.)

The reasonable time averaged electric force density is solved by plasma simulation. This force density is the source term in the Navier–Stokes equation to actuate the fluid flow shown in figure 5. Figure 5(*a*) shows that the electric force draws the fluid from the inlet on the left and drains the fluid upwards to the outlet at the top. The contour is coloured by the V_z-velocity component and shows the highest upward velocity close to the corner of the microplasma pump. We can see a vortex at the right boundary (symmetric plane) because the horseshoe actuator entrains the fluid from the top and pushes it from the right to the left and creates a plasma pinch. Figure 5(*b*) shows that the streamwise flow hits this plasma barrier at $x = 0.8$ mm. Figure 5(*a*) depicts two vortical structures near the inlet not found in our reported 2D simulation [10]. This is because in this 3D study, we consider the end effect along the y-direction shown in figure 5(*b*) which was missing in the 2D simulation.

4.2. Case 2: large opening with 80 V

Figure 6 shows the charge separation and the potential distribution with force vectors for case 2. We can see that the highest value of the charge separation increases due to the increase in the potential. The force vectors are still acting towards the grounded electrode due to the distribution of the electric field and the charge separation. For case 2, the highest applied voltage is 80 V, which matches the given boundary conditions as shown in figure 6(*b*).

Figure 7 shows the fluid stream traces at (*a*) $y = 0.3$ mm and (*b*) $z = 0.12$ mm. Figure 7(*a*) shows that the inlet vortices shown in figure 5(*a*) have been reduced due to the higher electric force than case 1. Also, the location of the actuators may be another factor. However, we can see a bigger vortical

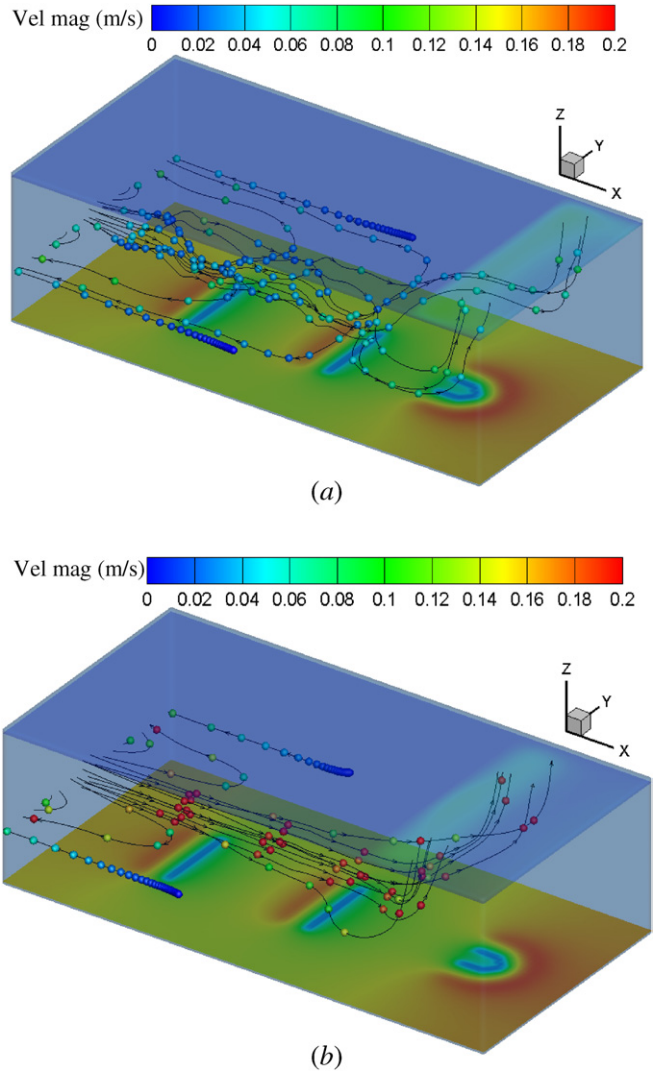

Figure 8. Fluid particles and top wall coloured with velocity magnitude (m s^{-1}); bottom wall coloured with potential ϕ (V) for (*a*) case 1 and (*b*) case 2. (Colour online.)

structure at the outlet because the horseshoe plasma actuator sucks more fluid from the outlet and pushes it back to the outlet and creates a clockwise vortical structure. Figure 7(*b*) shows that the fluid moves right along the x-direction and hits this clockwise plasma barrier at $x = 0.85$ mm. So the fluid momentum changes its direction upwards. It is obvious that the flow of case 2 is better than case 1 due to the fewer vortices inside the microplasma pump.

Figure 8 shows the comparison of fluid particles coloured by the velocity magnitude for (*a*) case 1 and (*b*) case 2 in the isometric view. The top wall is coloured by the velocity magnitude, while the bottom wall is coloured by the potential. So we can easily see the outlet and the location of the actuators. The average velocity magnitude at the outlet is 6.5 cm s^{-1} for case 2 which is faster than 4.4 cm s^{-1} in case 1. Also, the stream traces of fluid flow in case 2 are smoother than case 1. For the calculation of average flow rate Q, we find $Q_1 = 0.63$ ml min^{-1} (in case 1) and $Q_2 = 1.5$ ml min^{-1} (in case 2). Importantly, the predicted flow rate Q for the designs of case 2 produces the same level of flow rate in the literature [2] which may be useful for micropropulsion in space.

5. Conclusions

We have studied two cases of microplasma pumps using two-species 3D hydrodynamic plasma model coupled with the Possion equation. Both plasma governing equations and the Navier–Stokes equations are solved using a 3D finite element based MIG flow code. The results show the highest charge separation and force close to the powered electrodes. We find three vortical structures inside the pump which cannot be found in our 2D simulation. To reduce the vortices inside the microplasma pump, the location of the actuators and the input voltage may be key factors. The 3D flow simulation at 5 Torr predicts two orders of magnitude lower flow rate than those earlier predicted [10] for atmospheric condition. The predicted flow rate in case 2 ($Q_2 = 1.5$ ml min^{-1}) is about three times higher than that in case 1 ($Q_1 = 0.63$ ml min^{-1}). Such flow rates may be useful for micropropulsion in space. For the real case of micropump operating in air, the electron loss will be higher than the case in nitrogen [25]. This may produce much higher force resulting in a higher flow rate in air. Such a micropump will be quite useful for a range of practical applications from biology and medicine to microsatellite propulsion and microelectronics cooling [2, 3].

Acknowledgments

This work was partially supported by the AFOSR Grants monitored by Drs Douglas Smith and John Schmisseur. The authors also acknowledge partial support from the Florida Center for Advanced Aero-Propulsion (FCAAP) for this research.

References

[1] Thomas L J and Bessman S P 1975 Micropump powered by piezoelectric disk benders *US Patent* 3963380
[2] Laser D J and Santiago J G 2004 A review of micropumps *J. Micromech. Microeng.* **14** R35–64
[3] Oh K W and Ahn C H 2006 A review of microvalves *J. Micromech. Microeng.* **16** R13–39
[4] Roy S 2007 Method and apparatus for efficient micropumping *International Publication number* PCT International Publication WO 2009/015371
[5] Roth J R, Sherman D M and Wilkinson S P 1998 Boundary layer flow control with a one atmosphere uniform glow discharge surface plasma *36th AIAA Aerospace Sciences Meeting and Exhibit (Reno, NV, January 2002)* AIAA 98-0328
[6] Corke T C, Jumper E J, Post M L, Orlov D and McLaughlin T E 2002 Application of weakly-ionized plasmas as wing flow-control devices *40th AIAA Aerospace Sciences Meeting and Exhibit (Reno, NV, January 2002)* AIAA-2002-350
[7] Shyy W, Jayaraman B and Andersson A 2002 Modeling of glow discharge-induced fluid dynamics *J. Appl. Phys.* **92** 6434–43

[8] Roy S and Gaintonde D 2006 Force interaction of high pressure glow discharge with fluid flow for active separation control *Phys. Plasmas* **13** 023503
[9] Roy S and Wang C C 2009 Bulk fluid modification with horseshoe and serpentine plasma actuator *J. Phys. D: Appl. Phys.* **42** 032004
[10] Wang C C and Roy S 2009 Microscale plasma actuators for improved thrust density *J. Appl. Phys.* **106** 013310
[11] Hibbe L B, Sichler P, Schrader C, Lucas N, Gericke K H and Buttgenbach S 2005 High frequency glow discharges at atmospheric pressure with micro-structured electrode arrays *J. Phys. D: Appl. Phys.* **38** 510–517
[12] Torres J M and Dhariwal R S 1999 Electric field breakdown at micrometre separations *Nanotechnology* **10** 102–7
[13] Wilson C G, Gianchandani Y B, Arslanbekov R R, Kolobov V and Wendt A E 2003 Profiling and modeling of dc nitrogen microplasmas *J. Appl. Phys.* **94** 5
[14] Kushner M J 2004 Modeling of microdischarge devices: pyramidal structures *J. Appl. Phys.* **95** 3
[15] Sakiyama Y and Graves D B 2009 Neutral gas flow and ring-shaped emission profile in non-thermal RF-excited plasma needle discharge at atmospheric pressure *Plasma Sources Sci. Technol.* **18** 025022
[16] Boeuf J P, Pitchford L C and Schoenbach K H 2005 Predicted properties of microhollow cathode discharges in xenon *Appl. Phys. Lett.* **86** 071501
[17] Wang Q, Economou D J and Donnelly V M 2006 Simulation of a direct current microplasma discharge in helium at atmospheric pressure *J. Appl. Phys.* **100** 023301
[18] Radjenovic M R , Lee J K, Iza F and Park G Y 2005 Particle-in-cell simulation of gas breakdown in microgaps *J. Phys. D: Appl. Phys.* **38** 950–954
[19] Choi J, Iza F, Lee J K and Ryu C M 2007 Electron and ion kinetics in a DC microplasma at atmospheric pressure *IEEE Trans. Plasma Sci.* **35** 5
[20] Farouk T, Farouk B, Staack D, Gutsol A and Fridman A 2006 Simulation of DC atmospheric pressure argon micro glow-discharge *Plasma Sources Sci. Technol.* **15** 676–88
[21] Kumar H and Roy S 2005 Multidimensional hydrodynamic plasma–wall model for collisional plasma discharges with and without magnetic field effects *Phys. Plasmas* **12** 093508
[22] Surzhikov S T and Shang J S 2004 Two-component plasma model for two-dimensional glow discharge in magnetic field *J. Comput. Phys.* **199** 437–64
[23] Roy S, Raju R, Chuang H F, Cruden B A and Meyyappan M 2003 Modeling gas flow through microchannels and nanopores *J. Appl. Phys.* **93** 8
[24] Baker A J and Pepper D W 1991 *Finite Element 1–2–3* (New York: McGraw Hill)
[25] Singh K P and Roy S 2007 Modeling plasma actuators with air chemistry for effective flow control *J. Appl. Phys.* **101** 123308